Ab initio calculations of scattering cross sections of the three-body system $(\bar{p},e^+,e^-)$ between the $e^- + \bar{H}(n=2)$ and $e^- + \bar{H}(n=3)$ thresholds

Mateo Valdes,[*] Marianne Dufour,[†] and Rimantas Lazauskas[‡]
Université de Strasbourg, CNRS, IPHC UMR 7178, F-67000 Strasbourg, France

Paul-Antoine Hervieux[§]
Université de Strasbourg, CNRS, IPCMS UMR 7504, F-67000 Strasbourg, France

(Received 22 September 2017; published 31 January 2018)

The *ab initio* method based on the Faddeev-Merkuriev equations is used to calculate cross sections involving the $(\bar{p},e^+,e^-)$ three-body system, with an emphasis on antihydrogen formation ($\bar{H}$) via antiproton ($\bar{p}$) scattering on positronium. This system is studied in the energy range between the $e^- + \bar{H}(n=2)$ and the $e^- + \bar{H}(n=3)$ thresholds, where precisely calculated cross sections can be useful for future experiments (GBAR, AEGIS, etc.) aiming to produce antihydrogen atoms. A special treatment is developed to take into account the long-range charge-dipole interaction effect on the wave function. Emphasis is placed on the impact of Feshbach resonances and Gailitis-Damburg oscillations appearing in the vicinity of the $\bar{p} + \mathrm{Ps}(n=2)$ threshold.

DOI: 10.1103/PhysRevA.97.012709

I. INTRODUCTION

Within the framework of classical physics, gravity is described by the general theory of relativity (GR). The central issue of GR is the Einstein equivalence principle. Gravity may be considered an attractive force between massive bodies, and the weak equivalence principle (or universality of free fall) states that two massive test bodies fall in the same way independently of their compositions or their internal structures. For the standard matter this principle has been verified with the very high accuracy of 10^{-13} [1].

When quantum effects are considered, theories in the field of particle physics also include antimatter (Dirac equation, standard model, etc.). Their modern extensions do not exclude that the gravity force between matter and antimatter may differ from the force between similar massive bodies, thus violating the weak equivalence principle [2]. Some theories even speculate that antimatter has a negative mass that would consequently be repelled by matter. This property might explain the effects of dark energy and dark matter. So far no direct test has been done on the weak equivalence principle with antimatter.

In order to directly observe the effect of gravitation on antimatter, the aim of the GBAR experiment [3] is to measure the influence of Earth's gravitational field in the trajectory of antihydrogen atoms (see [4] for a recent account of the experiments on antimatter performed at CERN). In GBAR, antihydrogen atoms will be at rest before they undergo a free fall. This provided the name of the experiment: Gravitational Behaviour of Antihydrogen at Rest. The conception of the GBAR experiment is based on the original idea, proposed by Walz and Hänsch [5], of sympathetically cooling positive ions of antihydrogen, $\bar{H}^+$. The latter process is used in order to bring the ions almost to the resting state. Then one of the positrons is photodetached, thus leading to the production of neutral antihydrogen atoms, $\bar{H}$. The GBAR experiment follows three steps: (i) production of antihydrogen positive ions; (ii) their cooling, trapping, and photodetachment; and (iii) free fall of the neutral antihydrogen atoms.

In order to produce antihydrogen positive ions the following sequence of reactions is considered:

$$\begin{aligned} \bar{p} + \mathrm{Ps} &\rightarrow \bar{H} + e^-, \\ \bar{H} + \mathrm{Ps} &\rightarrow \bar{H}^+ + e^-, \end{aligned} \tag{1}$$

where $\bar{p}$ stands for antiproton, Ps for positronium (bound positron-electron pair), either in the ground state or in the excited state, $\bar{H}$ for antihydrogen (which can also be produced in the excited state), and e^- for electron. Let us stress that forming $\bar{H}$ by charge transfer from Ps is not a novelty of GBAR. The ATRAP experiment at CERN has already successfully produced $\bar{H}$ using this reaction [6]. Moreover, the AEGIS experiment plans to use the same reaction. The second reaction is a more complex collision process that we do not consider here.

One of the biggest challenges faced by GBAR is to find the best experimental and physical conditions (Ps state, antiproton energy, etc.) to enhance antihydrogen production. Along this line, in this work we focus on the scattering reactions of the three-body system $(\bar{p},e^+,e^-)$ in the energy region between the $e^- + \bar{H}(n=2)$ and the $e^- + \bar{H}(n=3)$ thresholds, with special emphasis on the first charge exchange reaction of GBAR. Moreover, as described below, special attention will be given to reactions exhibiting resonant behavior.

One of the most exciting phenomena in the scattering of charged particles with hydrogenlike atoms is the presence of Feshbach resonances that appear just *below* each energy threshold of the degenerate levels. Indeed, a charged particle moving in the field of an excited atom generates a dipole potential which couples the degenerate states and may lead

[*]mateovaldup@gmail.com
[†]marianne.dufour@iphc.cnrs.fr
[‡]rimantas.lazauskas@iphc.cnrs.fr
[§]hervieux@unistra.fr

to a long-range effective $1/y^2$ potential between the charged particle and the atom [7]. This potential gives rise to an infinite number of weak quasibound states whose energies form a logarithmic sequence in relation to the threshold. These states decay into lower-lying levels exhibiting the Feshbach resonance phenomenon. The presence of these resonances is well established both formally and quantitatively in a number of three-body Coulomb systems. For instance, resonances of this kind have already been found in antiproton-positronium collisions [8] and their presence might turn out to be important in boosting the antihydrogen production cross section, as originally pointed out in [9].

For the same three-body system and for energies just *above* the degenerate antihydrogen or positronium thresholds, a different phenomenon takes place. It was predicted by Gailitis and Damburg [7,10] in their calculation of the electron-hydrogen scattering system. It is often referred to as Gailitis-Damburg oscillations or Gailitis resonances. Gailitis and Damburg demonstrated that the presence of an effective $1/y^2$ attractive potential should generate near-threshold phase oscillations. Such oscillations are intimately related to the presence of the aforementioned quasibound states (Feshbach resonances) just below the degenerate thresholds in accordance with Levinson's theorem [11]. The latter relates the number of bound states of a potential to the difference in phase of a scattered wave at zero and infinite energies, leading to $\delta(E=0) - \delta(E\to\infty) = n\pi$, where n is the number of bound states. Accordingly, if Feshbach resonances may be considered as three-body bound states, near-threshold phase oscillations should appear. Therefore, the previous may be considered a consequence of Levinson's theorem.

Here we explore the first reaction in Eq. (1) by an *ab initio* method, which has already been widely explored within a large variety of theoretical models (see [12] and references therein). Concerning *ab initio* methods recently used, calculations between the $e^- + \bar{\mathrm{H}}(n=2)$ and the $e^- + \bar{\mathrm{H}}(n=3)$ energy thresholds have been performed using the Faddeev-Merkuriev (FM) equations in Refs. [9] and [13–15]. In the latter, the resonant behavior of the S-wave cross sections has been thoroughly discussed and total cross sections have also been presented, but only for a few energy values. Finally, partial and total cross sections for $\bar{\mathrm{H}}$ production have also been computed in a broader energy region within the framework of the two-center convergent close-coupling method [16–18].

In the present work, the FM equations are solved using the Lagrange-mesh method [19,20]. Special focus is on the role played by Feshbach and Gailitis resonances in the three-body reactions and, in particular, on the antihydrogen formation cross section, which is of interest to GBAR.

The main lines of the theory are given in the next section and the numerical techniques employed are detailed in Sec. III. In Sec. IV the results are presented, and a conclusion is given in Sec. V.

II. THEORETICAL FORMALISM

A. The Faddeev-Merkuriev equations

In the beginning of the 1960s Faddeev formulated a set of equations suited for solving nonrelativistic quantum three-particle scattering problems for short-range potentials [21]. Later, these equations were refined by Merkuriev [22] in order to treat three-particle Coulomb problems. The FM equations are constructed from the standard three-particle Hamiltonian, which, for the particular system $(\bar{p},e^+,e^-)$, may be expressed as

$$H_{\mathrm{lab}} = \frac{\mathbf{p}_{\bar{p}}^2}{2m_{\bar{p}}} + \frac{\mathbf{p}_{e^+}^2}{2m_e} + \frac{\mathbf{p}_{e^-}^2}{2m_e} - \frac{\alpha\hbar c}{|\mathbf{r}_{e^+} - \mathbf{r}_{e^-}|} - \frac{\alpha\hbar c}{|\mathbf{r}_{\bar{p}} - \mathbf{r}_{e^+}|} + \frac{\alpha\hbar c}{|\mathbf{r}_{\bar{p}} - \mathbf{r}_{e^-}|}; \quad (2)$$

here $\alpha = \frac{e^2}{4\pi\epsilon_0\hbar c}$ is the fine-structure constant, and m_p and m_e are, respectively, the proton and electron masses. The two-body interaction terms are represented by Coulomb potentials.

In order to separate the center-of-mass degrees of freedom, it is convenient to reformulate the problem using mass-scaled Jacobi coordinates $\{\mathbf{x}_i,\mathbf{y}_i\}$ (Fig. 1).

For a three-body system with masses m_i and position vectors $\mathbf{r}_i$, $(i=1,2,3)$, these coordinates are defined as

$$\mathbf{x}_i = \tau_i(\mathbf{r}_j - \mathbf{r}_k),$$
$$\mathbf{y}_i = \mu_i\left(\mathbf{r}_i - \frac{m_j\mathbf{r}_j + m_k\mathbf{r}_k}{m_j + m_k}\right), \quad (3)$$

where

$$\tau_i = \sqrt{2\frac{m_j m_k}{m_j + m_k}}, \quad \mu_i = \sqrt{2m_i\left(1 - \frac{m_i}{M}\right)},$$
$$M = m_i + m_j + m_k, \quad \text{where} \quad (i,j,k) = \mathrm{cyclic}(1,2,3). \quad (4)$$

There exist three equivalent sets of intrinsic coordinates $\{\mathbf{x}_i,\mathbf{y}_i\}$ (where $i=1,2,3$). Each coordinate set is associated with a three-particle configuration and is best suited to follow its evolution (Fig. 1). The terms μ_i and τ_i represent, respectively, the two-body and three-body reduced masses and M is the total mass of the system.

Two sets of Jacobi coordinates are related by the orthogonal transformation,

$$\begin{pmatrix}\mathbf{x}_j\\ \mathbf{y}_j\end{pmatrix} = \begin{pmatrix}c_{ji} & s_{ji}\\ -s_{ji} & c_{ji}\end{pmatrix}\cdot\begin{pmatrix}\mathbf{x}_i\\ \mathbf{y}_i\end{pmatrix}, \quad (5)$$

with

$$c_{ji} = -\left[\frac{m_j m_i}{(M-m_j)(M-m_k)}\right]^{1/2},$$
$$s_{ji} = (-)^{j-i}\,\mathrm{sgn}(i-j)\left(1 - c_{ji}^2\right)^{1/2}, \quad (6)$$

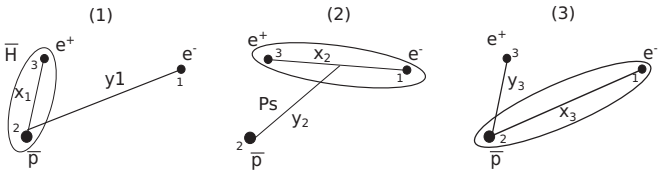

FIG. 1. The three possible configurations, where $\{\mathbf{x}_i,\mathbf{y}_i\}$ are the three possible sets of Jacobi coordinates.

where sgn$(i-j)$ is the sign of the subtraction $(i-j)$. In terms of Jacobi coordinates the Coulomb potentials are defined as

$$V_i(x_i) = \frac{z_j z_k \tau_i}{x_i}, \tag{7}$$

where z_j and z_k represent the physical charges of particles j and k, respectively, and $x_i = \mid \mathbf{x}_i \mid$, $y_i = \mid \mathbf{y}_i \mid$.

The FM equations are based on the proper decomposition of the Coulomb potentials into a short-range $V_i^{(s)}$ and a long-range $V_i^{(\ell)}$ part [23], which leads to

$$\begin{aligned} V_i^{(s)}(x_i,y_i) &= V_i(x_i)\chi^{(M)}(x_i,y_i), \\ V_i^{(\ell)}(x_i,y_i) &= V_i(x_i)[1-\chi^{(M)}(x_i,y_i)]. \end{aligned} \tag{8}$$

Here $\chi^{(M)}$ is a cutoff function defined by Merkuriev which tends to 0 in the asymptotic region where $x_i \to \infty$ (with $y_i \sim x_i$) and tends to 1 when $x_i \to 0$ or ($x_i \sim x_0$ and $y_i \to \infty$),

$$\chi^{(M)}(x,y) = 2\left[1+\exp\left(\frac{(x/x_0)^\nu}{y/y_0+1}\right)\right]^{-1}, \tag{9}$$

where x_0 and y_0 are two length parameters of free choice. However, their values must be chosen according to the dimensions of the two-body and three-body regions [23]. The value of the parameter ν must be chosen larger than 2. This separation leads to the FM equations,

$$\begin{aligned} &\left(E-H_0-V_1-V_2^{(\ell)}-V_3^{(\ell)}\right)F_1(\mathbf{x}_1,\mathbf{y}_1) \\ &\quad = V_1^{(s)}(F_2(\mathbf{x}_2,\mathbf{y}_2)+F_3(\mathbf{x}_3,\mathbf{y}_3)), \\ &\left(E-H_0-V_2-V_1^{(\ell)}-V_3^{(\ell)}\right)F_2(\mathbf{x}_2,\mathbf{y}_2) \\ &\quad = V_2^{(s)}(F_1(\mathbf{x}_1,\mathbf{y}_1)+F_3(\mathbf{x}_3,\mathbf{y}_3)), \\ &\left(E-H_0-V_3-V_1^{(\ell)}-V_2^{(\ell)}\right)F_3(\mathbf{x}_3,\mathbf{y}_3) \\ &\quad = V_3^{(s)}(F_1(\mathbf{x}_1,\mathbf{y}_1)+F_2(\mathbf{x}_2,\mathbf{y}_2)), \end{aligned} \tag{10}$$

where $F_i(\mathbf{x}_i,\mathbf{y}_i)$ are the FM components. Thus, the three-body wave function may be simply expressed as the sum of these three components:

$$\begin{aligned} \Psi(\mathbf{x},\mathbf{y}) = {} & F_1(\mathbf{x}_1(\mathbf{x},\mathbf{y}),\mathbf{y}_1(\mathbf{x},\mathbf{y})) + F_2(\mathbf{x}_2(\mathbf{x},\mathbf{y}),\mathbf{y}_2(\mathbf{x},\mathbf{y})) \\ & + F_3(\mathbf{x}_3(\mathbf{x},\mathbf{y}),\mathbf{y}_3(\mathbf{x},\mathbf{y})). \end{aligned} \tag{11}$$

Since only central potentials are considered here, the total angular momentum L is a good quantum number of the system. Therefore, the scattering problem can be split into a set of solutions for a fixed angular momentum quantum number. In order to numerically solve the FM equations we decompose each component into a partial-wave basis of total angular momentum LM and parity π, represented by the bipolar harmonics,

$$F_i^{LM,\pi}(\mathbf{x}_i,\mathbf{y}_i) = \sum_{\vec{\ell}_{x_i}+\vec{\ell}_{y_i}=\vec{L}} \frac{f^L_{\ell_{x_i}\ell_{y_i}}(x_i,y_i)}{x_i y_i}\left\{Y_{\ell_{x_i}}(\hat{x}_i)\times Y_{\ell_{y_i}}(\hat{y}_i)\right\}_{LM}, \tag{12}$$

where $\hat{x}_i$ and $\hat{y}_i$ are the angular parts of the vectors $\mathbf{x}_i$ and $\mathbf{y}_i$. $\{\ell_{x_i},\ell_{y_i}\}$ are the orbital momenta associated with $\mathbf{x}_i$ and $\mathbf{y}_i$, which satisfy $\vec{L} = \vec{\ell}_{x_i} + \vec{\ell}_{y_i}$. Within the case considered in this work we associate ℓ_{x_1} and ℓ_{x_2} with the orbital momenta of the antihydrogen and the positronium atoms, respectively. Finally $f^L_{\ell_{x_i}\ell_{y_i}}(x_i,y_i)$ is a function of the radial variables, corresponding to the set of quantum numbers $\{\ell_{x_i},\ell_{y_i},L\}$. To simplify further notation we define by α_i a set of partial angular momentum values $\{\ell_{x_i},\ell_{y_i}\}$ associated with configuration i. Therefore each value of α_i is associated with a couple of values $\{\ell_{x_i},\ell_{y_i}\}$. In the following we denote

$$Y^{LM}_{\alpha_i}(\hat{x}_i,\hat{y}_i) = \left\{Y_{\ell_{x_i}}(\hat{x}_i)\times Y_{\ell_{y_i}}(\hat{y}_i)\right\}_{LM}. \tag{13}$$

The projection of Eqs. (10) onto the bipolar spherical harmonics leads to a two-dimensional infinite set of integrodifferential equations. For a fixed total angular momentum the expression of the integrodifferential radial equations is given by

$$\sum_{\alpha_i'}\left(H_{\alpha_i,\alpha_i'}\delta_{\alpha_i,\alpha_i'} - \bar{V}^{(\ell)}_{\alpha_i\alpha_i'}\right)\frac{f^L_{\alpha_i'}(x_i,y_i)}{x_i y_i} = V_i^{(s)}(x_i,y_i)\left(\int_{-1}^{1} du_i \sum_{j\neq i=1}^{3}\sum_{\alpha_j'} h^L_{\alpha_i,\alpha_j'}(x_i,y_i,u_i)\frac{f^L_{\alpha_j'}(x_j,y_j)}{x_j y_j}\right), \tag{14}$$

with $u_i = (\mathbf{x}_i.\mathbf{y}_i)/(x_i y_i)$,

$$\begin{aligned} H_{\alpha_i,\alpha_i'} &= \left(E+\frac{\partial^2}{\partial x_i^2}+\frac{\partial^2}{\partial y_i^2}-\frac{\ell_{x_i}(\ell_{x_i}+1)}{x_i^2}-\frac{\ell_{y_i}(\ell_{y_i}+1)}{y_i^2}-V_i(x_i)\right), \\ \bar{V}^{(\ell)}_{\alpha_i\alpha_i'} &= \int d\hat{x}_i d\hat{y}_i Y^{LM*}_{\alpha_i}(\hat{x}_i,\hat{y}_i)\left(V_j^{(\ell)}+V_k^{(\ell)}\right)Y^{LM}_{\alpha_i'}(\hat{x}_i,\hat{y}_i), \end{aligned} \tag{15}$$

and

$$h^L_{\alpha_i,\alpha_j'}(x_i,y_i,u_i) = \int d\zeta_i d\vartheta_i d\phi_i Y^{LM*}_{\alpha_i}(\hat{x}_i,\hat{y}_i)Y^{LM}_{\alpha_j'}(\hat{x}_j,\hat{y}_j). \tag{16}$$

In the last expression integration is performed analytically over three Euler angles $(\zeta_i,\vartheta_i,\phi_i)$ chosen among the four Euler angles defining $(\hat{x}_i,\hat{y}_i)$ and where $d\hat{x}_i d\hat{y}_i = d\zeta_i d\vartheta_i d\phi_i du_i$.

We do not provide the full expression for a functional $h^L_{\alpha_i,\alpha_j'}(x_i,y_i,u_i)$, which might be found in [24] or in any handbook on few-body physics.

At low energy, only solutions for the smallest values of the total angular momentum quantum numbers are relevant, since all the physical observables converge rapidly once expanded in L. In the same manner one cuts expansion in the partial angular momentum values by limiting the maximally allowed value of ℓ_{x_i} and ℓ_{y_i} in the $\{\ell_{x_i},\ell_{y_i}\}$ expansion. In this work maximal values of the partial angular momenta were taken in the range $8 \leqslant \ell_{x_i} \leqslant 11$, $9 \leqslant \ell_{y_i} \leqslant 12$ and proved to be sufficient to get converged results.

B. Degenerated-state asymptotic wave functions

In order to incorporate proper boundary conditions, radial functions of the FM components are separated into two parts,

$$ {}^{\beta_j} f^{L}_{\alpha_i}(x_i,y_i) = {}^{\beta_j} f^{L,\mathrm{core}}_{\alpha_i}(x_i,y_i) + {}^{\beta_j} f^{L,\mathrm{as}}_{\alpha_i}(x_i,y_i); \tag{17}$$

here the index β_j indicates the initial scattering channel, and the term ${}^{\beta_j} f^{L,\mathrm{core}}_{\alpha_i}(x_i,y_i)$ represents the 'core' part of the FM component, which describes the system in the region with three particles close to each other. This term vanishes in the limit of large intercluster separation, when either x_i or y_i becomes large. Therefore this term can be efficiently described by a linear expansion into a set of square-integrable basis functions. The term ${}^{\beta_j} f^{L,\mathrm{as}}_{\alpha_i}(x_i,y_i)$ is added to account for the relative motion of a particle i with respect to a bound cluster of particle jk in the asymptotic region $y_i \to \infty$. This term includes both incoming and outgoing scattering waves, having the general structure

$$ {}^{\beta_j} f^{L,\mathrm{as}}_{\alpha_i}(x_i,y_i) = f^{\mathrm{reg}}_i(y_i) \sum_{\beta_o,\beta_m} \phi^{\mathrm{bs}}_{n_i,\ell_{x_i}}(x_i) g^{\beta_o}_{\beta_m}(y_i) \times \delta_{\beta_m \subset \alpha_i} \delta_{n_i \subset \beta_o, n_i \subset \beta_m}, \tag{18}$$

where summation runs only over open channels (β_o,β_m) in the scattering process. The index β_o represents a set of three quantum numbers $\{n_o,\ell_{x_o},\ell_{y_o}\}$ defining open scattering channels. $\phi^{\mathrm{bs}}_{n_i,\ell_{x_i}}$ is the reduced radial function of the two-body system, whereas $g^{\beta_o}_{\beta_m}$ is the relative radial function describing the behavior between the two-body system and the third particle. The latter expression is premultiplied by a function $f^{\mathrm{reg}}_i(y_i) = (1-\exp(-y_i/y_{\mathrm{reg}}))^n$ aiming to rend it regular at small y_i values. When the open channel is energy nondegenerate ($n_o = 1$, but also $n_o = 2$ case for nonnatural parity states) the term $g^{\beta_o}_{\beta_m}$ contains a single component $\beta_o = \beta_m$ and is described in a standard way combining Riccati-Bessel and Riccati-Neumann functions.

However, Bessel functions do not match y asymptotes of the energy-degenerate states. This is mostly due to the presence of charge-dipole interaction terms $\sim 1/y_i^2$, coupling different energy-degenerate states. To solve the latter problem the term $g^{\beta_o}_{\beta_m}$ is developed using distorted waves, based on the auxiliary potential $\bar{\bar{V}}_{\beta'_m,\beta_m}(y_i)$ at long range including the appropriate dipole $1/y_i^2$ and quadrupole $1/y_i^3$ terms. At short range this potential is forced to fade away, allowing numerical determination of the distorted-wave regular $g^{\beta_o}_{\beta_m,R}(y_i)$ and irregular $g^{\beta_o}_{\beta_m,I}(y_i)$ solutions. In practice, one may see that the right-hand side of Eq. (14) is effectively 0 at long range, therefore an efficient auxiliary potential should mimic the term $\bar{V}^{(\ell)}_{\alpha_i\alpha'_i}$. Keeping this in mind, independent distorted-wave solutions $g^{\beta_o}_{\beta_m}(y_i)$ are constructed by projecting the left-hand side of Eq. (14) onto the set of antihydrogen (or positronium) bound-state wave functions, representing an energy-degenerate channel ($n_i > 1$). This projection gives a finite set of one-dimension radial equations which have to be solved,

$$ \left(H_{\beta'_m,\beta_m}\delta_{\beta'_m,\beta_m} - \sum_{\beta'_m} \bar{\bar{V}}_{\beta'_m,\beta_m} \right) g^{\beta_o}_{\beta_m,(\mathrm{I/R})}(y_i) = 0, \tag{19}$$

where

$$ H_{\beta'_m,\beta'_m} = k^2_{\beta'_m} + \frac{\partial^2}{\partial y_i^2} - \frac{\ell_{\beta'_m}(\ell_{\beta'_m}+1)}{y_i^2}, \tag{20}$$

and

$$ \bar{\bar{V}}_{\beta'_m,\beta_m}(y_i) = \int dx_i \phi^{\mathrm{bs}}_{n_o,\ell_{x_i}\subset\beta_m}(x_i) \overline{V}_{\ell_{y_i}\subset\beta_m,\ell_{y_j}\subset\beta'_m} \times (x_i,y_i) \phi^{\mathrm{bs}}_{n_o,\ell_{x_j}\subset\beta'_m}(x_i); \tag{21}$$

here k_{β_m} is the relative-mass-scaled momentum in channel β_m, $k^2_{\beta_m} = E_{3b} - E^{\beta_m}_{2b}$, E_{3b} is the energy of the three-body system in the center-of-mass frame, and $E^{\beta_m}_{2b}$ the bound energy of the two-body system of channel β_m.

For example, the effective potential $\bar{\bar{V}}_{\beta'_m,\beta_m}(y_i)$ shape between the ($n = 2$) degenerated channels is

$$ \bar{\bar{V}}_{\beta'_m,\beta_m}(y_i \to \infty) = \frac{A_{\beta'_m,\beta_m}}{y_i^3} \quad \text{if} \quad \ell'_{x_m} \subset \beta'_m = \ell_{x_m} \subset \beta_m = 1, \tag{22}$$

$$ \bar{\bar{V}}_{\beta'_m,\beta_m}(y_i \to \infty) = \frac{B_{\beta'_m,\beta_m}}{y_i^2} \quad \text{if} \quad \ell'_{x_m} \subset \beta'_m \neq \ell_{x_m} \subset \beta_m, \tag{23}$$

where $A_{\beta'_m,\beta_m}$ and $B_{\beta'_m,\beta_m}$ are real constants. In contrast with the work of Hu *et al.* [9], where only the dipole term has been considered, our calculations take into account higher order corrections. Between these degenerated states and the other states the coupling is due to second-order perturbation and effectively gives rise to polarization terms, which behave as $1/y_i^4$.

As a consequence, to construct $g^{\beta_o}_{\beta_m,(I/R)}(y_i)$ solutions used to approximate asymptotes of FM components, we solve a set of one-dimensional second-order differential equations (19). Due to triangular conditions that the set of quantum numbers $\beta_o \equiv \{n_o,\ell_{x_o},\ell_{y_o}\}$ should satisfy, the number of coupled equations is $1 \leqslant N \leqslant 3$ for $n_m \leqslant 2$. In particular, for the case $n_m = 2$ with natural parity $\pi = (-)^L$ and $L > 2$, the energy-degenerate open channels are $\beta_o \equiv \{2,0,L\},\{2,1,L-1\},\{2,1,L+1\}$. For a system of N-coupled equations one has to consider each channel separately as an initial free wave in the limit $y_i \to \infty$. Solving these equations is rather easy and is realized by integrating equations from $y_i = \infty$ to 0 using the Numerov method. As the plane wave is distorted by the long-range coupling terms, one gets N independent regular and irregular functions for all degenerated channels. Thus, a total of $N \times N$ regular and $N \times N$ irregular functions are to be obtained for a system of N-coupled equations.

Finally, the FM components in asymptotic regions are required to satisfy the boundary condition

$$
\begin{aligned}
&{}^{\beta_j} f^{L}_{\alpha_i}(x_i, y_i \to \infty) \\
&= \sum_{\beta_o,\beta_m} \phi^{\mathrm{bs}}_{n_i,\ell_{x_i}\subset\beta_m}(x_i)\left[g^{\beta_o}_{\beta_m,R}(y_i)\delta_{\beta_j,\beta_o} + \tilde{K}_{\beta_j\beta_m} g^{\beta_o}_{\beta_m,I}(y_i)\right] \\
&\quad \times \delta_{n_o\subset\beta_o,n_m\subset\beta_m}\delta_{\beta_m\subset\alpha_i},
\end{aligned}
\tag{24}
$$

where ${}^{\beta_j} f^{L}_{\alpha_i}(x_i, y_i)$ is the radial function for the α_i partial wave when the entrance channel is β_j. The sum over β_m and β_o runs only over open channels.

III. NUMERICAL METHOD

The radial parts of the 'core' terms of the FM components are approximated using Lagrange-Laguerre basis functions, implemented via the Lagrange-mesh method [19,20]. It reads

$$
f^{L,\mathrm{core}}_{\alpha_i} = \sum_{i_x,i_y}^{N_x,N_y} C_{\alpha_i,i_x,i_y} h_{i_x}(x_i) h_{i_y}(y_i). \tag{25}
$$

These Lagrange-Laguerre mesh functions are defined as

$$
\begin{aligned}
h_{i_x}(x) = (-1)^{i_x} c_{i_x}^{1/2} \frac{L^{\alpha}_{N_x}(x/\eta_x)}{x/\eta_x - x_{i_x}} x_{i_x}^{\alpha/2} \left(\frac{x/\eta_x}{x_{i_x}}\right)^{1/2} \\
\times \exp(-x/2\eta_x);
\end{aligned}
\tag{26}
$$

here $L^{\alpha}_{N_x}$ is a Laguerre polynomial of order N_x and $\{x_{i_x}\} = \{x_1, x_2, \ldots, x_{N_x}\}$ represents the set of its roots; in this work α is chosen equal to 1. The parameter η_x is used to adjust the range of the basis functions. The coefficients c_{i_x} are fixed to satisfy the orthonormality condition,

$$
\int_0^{\infty} h_{i_x} h_{i'_x} dx = \delta_{i_x i'_x}. \tag{27}
$$

As detailed in [20] using the Gauss quadrature approximation with N_x knots all the required integrals by the variational calculation are easily estimated [20]. A similar parametrization is used to express the functional dependence of FM components on the variable y_i; the scaling parameter η_x and number of mesh points may be chosen different for each grid.

To determine linear coefficients related to the expansion, (25), we project Eq. (15) onto the basis of the Lagrange-Laguerre functions, getting a set of linear equations,

$$
(\hat{H}_{\mathrm{FM}} - E_{3b})\tilde{C}^{\beta_o,(\mathrm{I/R})}_{\alpha_i,i_x,i_y} = b_{\beta_o,(I/R)}. \tag{28}
$$

Here $(\hat{H}_{\mathrm{FM}} - E_{3b})$ is a matrix, due to the projection of Eq. (15). The last set of linear equations is solved $2N_o$ times, by constructing the inhomogeneous term $b_{\beta_o,(\mathrm{I/R})}$ based on expression (18), generated either with the regular $g^{\beta_o}_{\beta_m,(R)}(y_i)$ or with the irregular distorted wave $g^{\beta_o}_{\beta_m,(I)}(y_i)$, where N_o is the number of open channels considered at E_{3b} energy.

To determine the K-matrix elements from the $2N_o$ independent solutions $\tilde{C}^{\beta_o,(I/R)}_{\alpha_i,i_x,i_y}$ we resort to the Wronskian relation, involving regular and irregular distorted waves. Actually, we dispose of two independent procedures. One is based on validating the Wronskian relation for the separate FM components,

$$
\begin{aligned}
K^{c}_{\beta_j\beta_m} = \frac{1}{\sqrt{k_{\beta_j} k_{\beta_m}}} \Big(\big\langle {}^{\beta_j} F^{LM}_{k,R} \big| \hat{H}_0 \big| {}^{\beta_m} F^{LM}_{i} \big\rangle \\
- \big\langle {}^{\beta_m} F^{LM}_{i} \big| \hat{H}_0 \big| {}^{\beta_j} F^{LM}_{k,R} \big\rangle \Big) \delta_{\beta_m\subset i}\delta_{\beta_j\subset k}.
\end{aligned}
\tag{29}
$$

The second choice is to validate the Wronskian relation for the total wave function

$$
\begin{aligned}
K^{c}_{\beta_j\beta_m} = \frac{1}{\sqrt{k_{\beta_j} k_{\beta_m}}} \Big(\big\langle {}^{\beta_j} F^{LM}_{k,R} \big| \hat{H}_0 \big| {}^{\beta_m} \Psi^{LM} \big\rangle \\
- \big\langle {}^{\beta_m} \Psi^{LM} \big| \hat{H}_0 \big| {}^{\beta_j} F^{LM}_{k,R} \big\rangle \Big) \delta_{\beta_j\subset k}.
\end{aligned}
\tag{30}
$$

In these equations ${}^{\beta_j} F^{LM}_{k,R}$ indicates the 'nonscattered' three-body wave function, based on the distorted-regular solution β_j, which belongs to particle channel k:

$$
\begin{aligned}
{}^{\beta_j} F^{LM}_{k,R,\alpha_i}(x_i, y_i) = \sum_{\beta_o,\beta_m} \phi^{\mathrm{bs}}_{n_i,\ell_{x_i}\subset\beta_m}(x_i) g^{\beta_o}_{\beta_m,R}(y_i)\delta_{\beta_j,\beta_o} \\
\times \delta_{n_o\subset\beta_o,n_m\subset\beta_m}\delta_{\beta_m\subset\alpha_i}.
\end{aligned}
\tag{31}
$$

In fact, the second procedure described in Eq. (30) corresponds to the standard Kohn variational functional (see Kievsky *et al.* [25] for a more thorough discussion). The first procedure, Eq. (29), is sometimes referred to as the Faddeev form of the Kohn variational functional [26].

The K^c matrix describes projection of the wave function asymptotes onto the distorted waves and thus depends on the choice of the auxiliary potentials for the degenerated states. In order to calculate the scattering observables it is convenient to transform this matrix into the conventional K matrix or S matrix, describing projection of the wave function asymptotes onto free waves. To this aim, first, the S^c matrix is determined in terms of the K^c matrix,

$$
S^c = \frac{(1 + iK^c)}{(1 - iK^c)}. \tag{32}
$$

Second, the disturbed-wave dependence of S^c is corrected,

$$
S = \tilde{S}^{1/2} S^c \tilde{S}^{1/2}, \tag{33}
$$

where $\tilde{S}$ is the matrix obtained for the interaction used to construct distorted waves. Thus, the K matrix is finally obtained:

$$
K = \frac{(S-1)}{i(S+1)}. \tag{34}
$$

The expression of the differential cross sections between the incoming channel i and the outgoing channel j as a function of the conventional K-matrix elements is given by

$$
\frac{d\sigma_{ij}}{d\Omega} = \frac{\pi a_0^2}{k_i^2} \left| \sum_L \frac{(2L+1)}{(2\ell_i+1)} \left(\frac{2K_L}{1 - iK_L}\right)_{ij} P_L(\cos(\theta)) \right|^2, \tag{35}
$$

where a_0 is the Bohr radius, k_i the relative momentum, ℓ_i the orbital momentum of the two-body system in the incoming channel i, P_L is the Legendre polynomial, and θ is the relative scattering angle. K_L is the K matrix for the L partial wave. The

partial cross sections are given by

$$\sigma_{ij}^{L} = \frac{\pi a_0^2}{k_i^2}\frac{(2L+1)}{(2\ell_i+1)}\left|\left(\frac{2K_L}{1-iK_L}\right)_{ij}\right|^2. \tag{36}$$

The total cross section is the sum of the partial cross sections,

$$\sigma_{ij}^{T} = \sum_{L}\sigma_{ij}^{L}. \tag{37}$$

To obtain all the results presented in the next section the calculations were realized on a supercomputer. In all the figures, circles represent the exact values obtained with our calculations. In the present results, the sum over angular momenta $\{\ell_x,\ell_y\}$ is truncated according to $8 \leqslant \ell_x^{\max} \leqslant 11$ and $9 \leqslant \ell_y^{\max} \leqslant 12$. The numbers of points (symbols) used in the Lagrange-Laguerre grid are $45 \leqslant N_x \leqslant 75$ and $60 \leqslant N_y \leqslant 75$. With these considerations, one is led to solve the linear algebra problem of 10^5 to 10^6 equations. The final matrix of the linear algebra problem is almost full, however, its matrix elements can be reproduced online from the elements of considerably smaller matrices prestored on the computer's RAM. In order to avoid storage of the final linear algebra problem matrix but also to speed up the solution, iterative linear algebra methods like BiCGSTAB(L) are used. For the numerical methods employed in this work one may refer to [27]. With these adjustments execution of the code does not require large amounts of RAM and can succeed even on a personal computer. However, the calculations can be time-consuming and therefore the code has been parallelized and mostly executed at computer centers. To compute the cross section for one energy value, the calculation can last between 2 and 18 h, depending on the energy and total orbital momentum considered. Because of the calculation time, we were obliged to limit the number of calculated energies. The energy values were chosen to highlight the general behavior of the cross sections as well as some narrow resonances. The solid lines in the figures correspond to the fit of the calculated results, aiming to show the general trend of the cross section. On average there are about 30 different energies for each partial wave. Most of the points (symbols) are chosen in the areas of resonances to describe their behavior. In these areas there is no fit.

IV. RESULTS

The results are presented in three parts. The first part (A) reports partial cross sections; the second (B), total cross sections; and the third (C), differential cross sections. In all figures, the thresholds are delimited by dotted vertical lines and their notation is defined as follows:

$$\begin{aligned} e^- + \bar{\mathrm{H}}(n=2) &\equiv \bar{\mathrm{H}}(2),\\ \bar{p} + \mathrm{Ps}(n=2) &\equiv \mathrm{Ps}(2),\\ e^- + \bar{\mathrm{H}}(n=3) &\equiv \bar{\mathrm{H}}(3). \end{aligned} \tag{38}$$

A. Partial cross sections

1. Results between the $\bar{\mathrm{H}}(n=2)$ and the $\mathrm{Ps}(n=2)$ thresholds

The closeness of Feshbach resonances to the threshold as well as their extremely small widths, representing less than a thousandth of the respective energy position, makes it a challenge to find and identify them in the calculated or, especially, the measured cross sections [28]. This phenomenon is highlighted in Fig. 2; for antiproton-positronium scattering we present the S-wave partial cross section of $\bar{\mathrm{H}}(2s,2p)$ production in $\bar{p} + \mathrm{Ps}(1s)$ collisions. Note that in all figures, symbols always represent the calculated values, whereas curves are added to guide the eye, representing smoothing of the calculated values by a least-squares fit. The antihydrogen production cross section is extremely small in S waves, representing $\sim$1% of the total cross section. It is determined from the vanishing nondiagonal S-matrix elements, being strongly influenced by any numerical inaccuracies. This is the reason why the calculated values in Figs. 2 and 3 deviate from the smooth curve. The size of these deviations allows one to estimate the accuracy of the final calculation. Notably, these numerical inaccuracies are no longer visible in the elastic scattering cross section, shown in Fig. 4, representing the dominant process in S waves, or in the total antihydrogen production

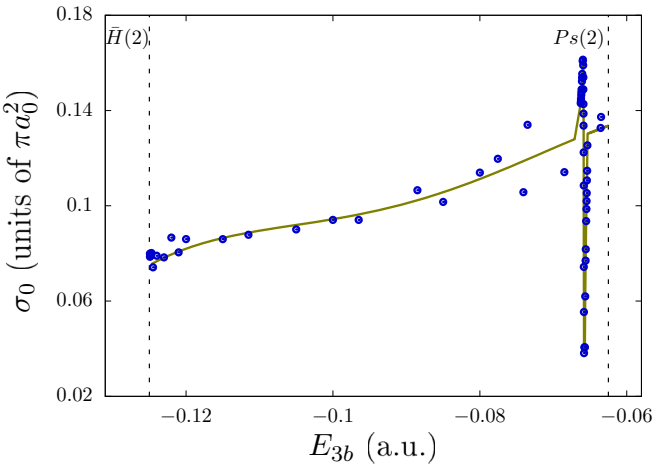

FIG. 2. S-wave partial cross section of the reaction $\bar{p} + \mathrm{Ps}(n = 1) \to e^- + \bar{\mathrm{H}}(n = 2)$. Vertical lines labeled $\bar{\mathrm{H}}(2)$ and Ps(2) indicate, respectively, the positions of the $\bar{\mathrm{H}}(n = 2)$ and $\mathrm{Ps}(n = 2)$ thresholds.

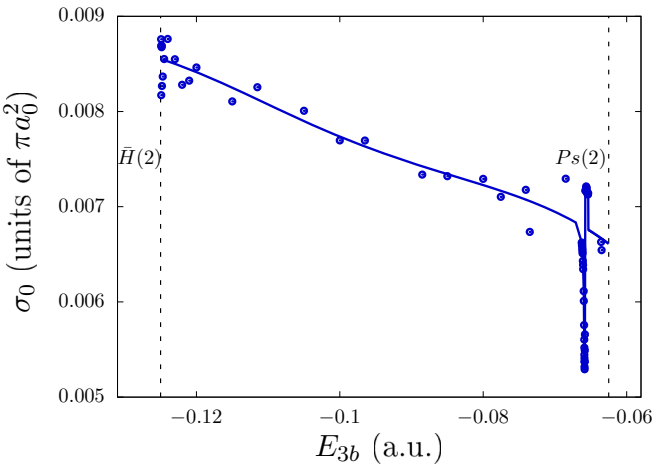

FIG. 3. S-wave partial cross section of the reaction $\bar{p} + \mathrm{Ps}(n = 1) \to e^- + \bar{\mathrm{H}}(n = 1)$.

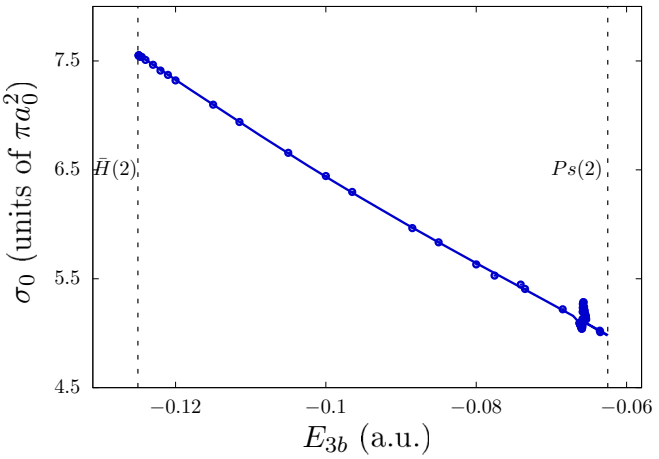

FIG. 4. S-wave partial cross section of the reaction $\bar{p} + \mathrm{Ps}(n = 1) \rightarrow \bar{p} + \mathrm{Ps}(n = 1)$.

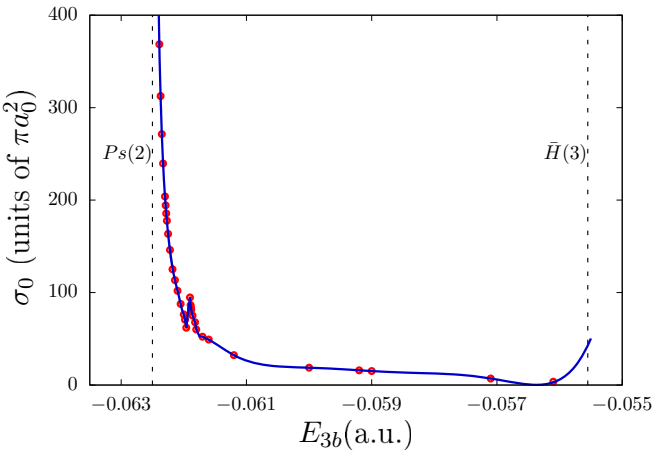

FIG. 6. S-wave partial cross section of the reaction $\bar{p} + \mathrm{Ps}(n = 2) \rightarrow e^- + \bar{\mathrm{H}}(n \leqslant 2)$.

cross section (Fig. 11), dominated by better-balanced higher partial waves.

In Fig. 2 one can identify a Feshbach resonance at $E_{3b} = -0.065\,83$ a.u., where E_{3b} is the energy of the three-body system in the center-of-mass frame. This energy position as well as its approximate width, $\Gamma/2 = 8 \times 10^{-5}$ a.u., are in good agreement with the direct calculations of the resonance parameters based on the complex scaling method [8,29]. The resonant behavior can also be observed in the S-wave partial cross sections of the associated processes in the same energy position, i.e., in $\bar{\mathrm{H}}(1s)$ production in $\bar{p} + \mathrm{Ps}(1s)$ collisions (Fig. 3) and in $\bar{p} + \mathrm{Ps}(1s)$ elastic scattering (Fig. 4).

In Fig. 5 the P-wave partial cross section of $\bar{\mathrm{H}}(2s,2p)$ production in $\bar{p} + \mathrm{Ps}(1s)$ collisions is shown. The $\bar{\mathrm{H}}(2s,2p)$ production is obtained by summing the contribution coming from the three degenerated channels. In addition to the antihydrogen production in its first excited state $\bar{\mathrm{H}}(2s,2p)$, the production of each degenerated channel—[$\bar{\mathrm{H}}(2s)$, $\ell_{y_1} = L$], [$\bar{\mathrm{H}}(2p)$, $\ell_{y_1} = L - 1$], and [$\bar{\mathrm{H}}(2p)$, $\ell_{y_1} = L + 1$)]—is also plotted. In this partial wave we are able to identify another Feshbach resonance with an energy position of $E = -0.074\,071\,9$ a.u. There is still a very good agreement between the resonance energy position and the results of Umair *et al.* [29] obtained with the complex scaling method.

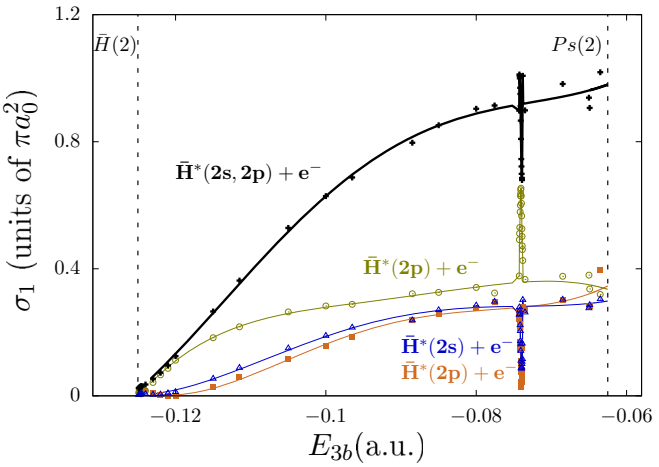

FIG. 5. P-wave partial cross sections of the reaction $\bar{p} + \mathrm{Ps}(n = 1) \rightarrow e^- + \bar{\mathrm{H}}(n = 2)$, separated to show the production of the different degenerate channels.

2. *Results between the* $\mathrm{Ps}(n = 2)$ *and the* $\bar{\mathrm{H}}(n = 3)$ *thresholds*

The presence of Gailitis-Damburg oscillations have only recently been demonstrated in full three-body calculations of $\bar{p} + \mathrm{Ps}(2s,2p)$ collisions [9,16–18]. Nevertheless, some ambiguities remain if these oscillations are able to influence antihydrogen production in the near-threshold region. In the first work by Hu *et al.* [9], based on FM equations, an important enhancement of the $\bar{p} + \mathrm{Ps}(2s,2p) \rightarrow \bar{\mathrm{H}}(1s,2s,2p) + e^-$ cross section was observed in the S partial wave. On the contrary, in a later work, by Kadyrov *et al.* [16], using the two-center convergent closed-coupling method, this enhancement is not confirmed and only the typical near-threshold behavior as k_i^{-2} [30] of the inelastic cross section is affirmed, where k_i is the incoming relative momentum between Ps and $\bar{p}$ in the incoming channel.

To clarify this issue we concentrate on $\bar{p} + \mathrm{Ps}(2s,2p)$ collisions just above the $\mathrm{Ps}(2s,2p)$ threshold. In Fig. 6 the S-wave partial cross section of $\bar{\mathrm{H}}(1s,2s,2p)$ production in $\bar{p} + \mathrm{Ps}(2s,2p)$ collisions is presented. A Gailitis-Damburg oscillation can be observed with energy position $E_{3b} = -0.06194$ a.u. The maximum of $94\pi a_0^2$ is determined at $E_{3b} = -0.061\,90$ a.u. These values are in good agreement with those of Hu *et al.* [9]. The position of our maximum differs from theirs by merely 8.0×10^{-5} a.u. On the contrary, we do not confirm the existence of the largest resonance observed by Hu *et al.* [6]. In this figure the cross section has the standard near the threshold k_i^{-2} behavior in accordance with [16] and [30].

In accordance with the work of Hu *et al.* [14], we have observed two phase-shift jumps for the S partial wave. One of these jumps is related to the oscillation previously discussed. The other one is situated very close to the threshold and does not lead to a visible resonant behavior in our S-wave partial cross section.

In Fig. 7 the S-wave partial cross section of $\bar{p} + \mathrm{Ps}(2s,2p)$ elastic scattering is plotted as a function of the relative energy

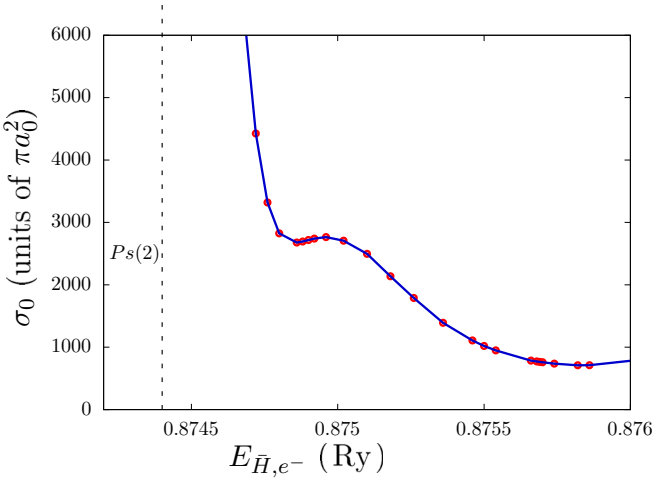

FIG. 7. S-wave partial cross section of the reaction $\bar{p} + \mathrm{Ps}(2s,2p) \rightarrow \bar{p} + Ps(2s,2p)$.

in the $e^- + \bar{\mathrm{H}}(1s)$ channel, $E_{\bar{\mathrm{H}}(1s),e^-} = E_{3b} + E_{\bar{\mathrm{H}}(1s)}$. In Fig. 8 the S-wave partial cross section of elastic scattering is shown separately for the Ps($2s$) and Ps($2p$) states. This result seems to be in strong disagreement with previous work [14]. In comparison to mentioned results, the cross sections of the separated Ps($2s$) and Ps($2p$) states are inverted. In addition, the cross-sections values are substantially different even if the energy positions of Gailitis-Damburg oscillations are in good agreement. As the Ps($2s$) and Ps($2p$) states present long-range coupling, to do a more rigorous comparison one should compare results obtained for $\bar{p} + \mathrm{Ps}(2s,2p)$ elastic scattering. Unfortunately this cross section is not given in Ref. [14].

In Fig. 9 the P-wave partial cross section of antihydrogen $\bar{\mathrm{H}}$ excitation via e^- scattering is given. A Gailitis-Damburg oscillation can be observed near the Ps(2) threshold. Such oscillation has never been observed in previous work. However, this oscillation has a negligible influence on the total cross section of antihydrogen $\bar{\mathrm{H}}$ excitation via e^- scattering and it is not noticeable in the antihydrogen $\bar{\mathrm{H}}$ production cross sections.

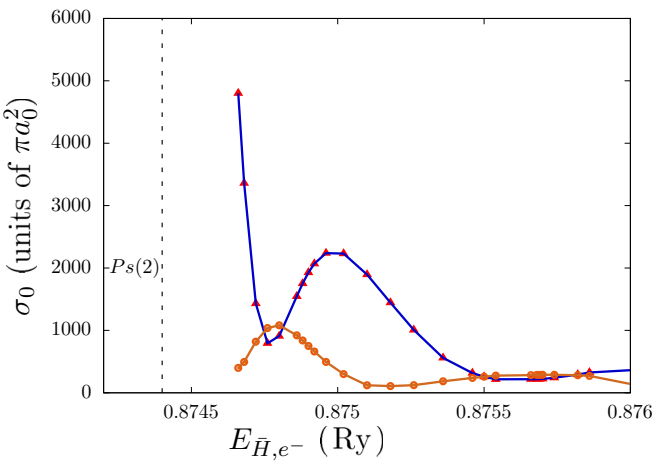

FIG. 8. S-wave partial cross sections of the reactions $\bar{p} + \mathrm{Ps}(2s) \rightarrow \bar{p} + \mathrm{Ps}(2s)$ (triangles) and $\bar{p} + \mathrm{Ps}(2p) \rightarrow \bar{p} + \mathrm{Ps}(2p)$ (circles).

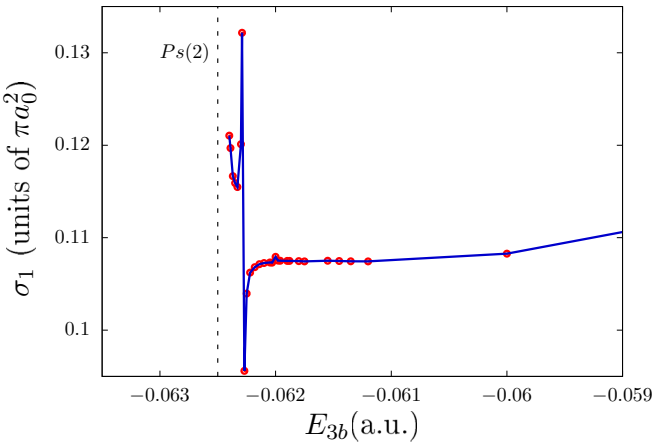

FIG. 9. P-wave partial cross section of the reaction $e^- + \bar{\mathrm{H}}(n = 1) \rightarrow e^- + \bar{\mathrm{H}}(n = 2)$.

Figure 10 presents the D-wave partial cross section for the $\bar{\mathrm{H}}(1s,2s,2p)$ formation in $\bar{p} + \mathrm{Ps}(2s,2p)$ collisions. For the first time two Gailitis-Damburg oscillations can be observed at $E_{3b} = -0.062\,22$ a.u. and at $E_{3b} = -0.061\,75$ a.u. These oscillations have not been pointed out in other works, in particular, in Refs. [9] and [15], where some values of this partial cross section are presented.

In Table I, the S-wave partial-cross-section values for three energies are compared to the results obtained by Hu *et al.* using the Faddeev-Merkuriev equations [32] and the results obtained by Papp *et al.* [31]. A good agreement with both works is observed. In the present work the results are obtained for a finite proton mass, $m_p = 1836.1515$ a.u.

B. Total cross sections

1. Results between the $\bar{\mathrm{H}}(n = 2)$ *and the* Ps($n = 2$) *thresholds*

In Fig. 11, the total antihydrogen production $\bar{\mathrm{H}}(1s,2s,2p)$ in $\bar{p} + \mathrm{Ps}(1s)$ collisions is plotted between the $\bar{\mathrm{H}}(2)$ and the $\bar{\mathrm{H}}(3)$ thresholds. The solid line represents the results obtained by summing the contribution of the partial cross sections for a total angular momentum lying within $0 \leqslant L \leqslant 7$. Crosses represent

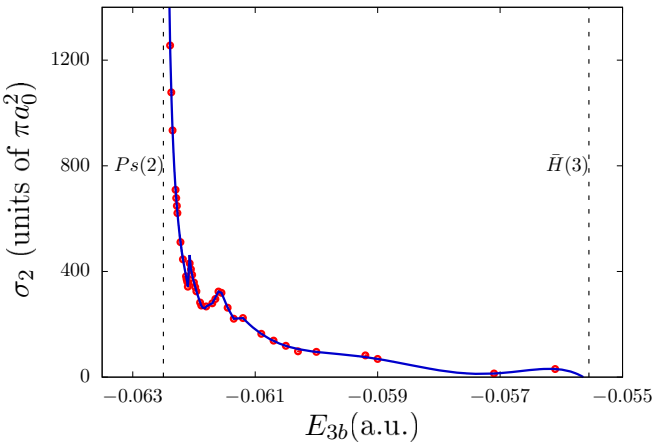

FIG. 10. D-wave partial cross section of the reaction $\bar{p} + \mathrm{Ps}(n = 2) \rightarrow e^- + \bar{\mathrm{H}}(n \leqslant 2)$.

TABLE I. Comparison of partial cross sections ($L = 0$) with the FM calculations of Hu *et al.* [9] and the results obtained by Papp *et al.* [31]. Channel 1 corresponds to $e^- + \bar{\mathrm{H}}(1s)$; channel 2 to $\bar{p} + \mathrm{Ps}(1s)$; and channel 3 to $e^- + \bar{\mathrm{H}}(2s,2p)$. σ_{11} is the elastic cross section of channel 1; σ_{12} and σ_{13} are, respectively positronium formation and the $\bar{\mathrm{H}}$ excitation cross sections.

E_{cm}	Ref. No.	σ_{11}	σ_{13}	σ_{12}
−0.115 a.u.	[9]	0.0900	0.001156	0.00572
	[31]	0.0951	0.001004	0.00558
	This work	0.0964	0.000891	0.00570
−0.10 a.u.	[9]	0.096	0.001514	0.00585
	[31]	0.1010	0.001641	0.00563
	This work	0.1015	0.001675	0.00574

the results obtained by Kadyrov *et al.* based on the two-center convergent close-coupling method [16]. The most important contributions at higher energies come from the D, F, and G partial waves, whereas the P, D, and F partial waves dominate at low energies.

There is a very good agreement between both results, yet the points provided by the two-center convergent close-coupling calculations do not scan the regions of narrow Feshbach resonances.

The K matrix allows us to determine the complete information about the scattering process, i.e., to extract the cross sections of elastic, excitation, and transfer reactions which can take place between the $\bar{\mathrm{H}}(n = 2)$ and the $\bar{\mathrm{H}}(n = 3)$ thresholds. For example, we present in Fig. 12 the total antihydrogen excitation cross section between the $\bar{\mathrm{H}}(2)$ and the Ps(2) thresholds. The P-wave resonance makes a pronounced contribution to this cross section. Indeed, the P, D, and F partial waves dominate this process, whereas the contribution of the S-wave resonance is suppressed by its low statistical weight.

As stated previously we took into account the partial-wave expansion up to the $L = 7$ partial wave. This truncation is justified as the contribution of the $L = 7$ partial wave drops

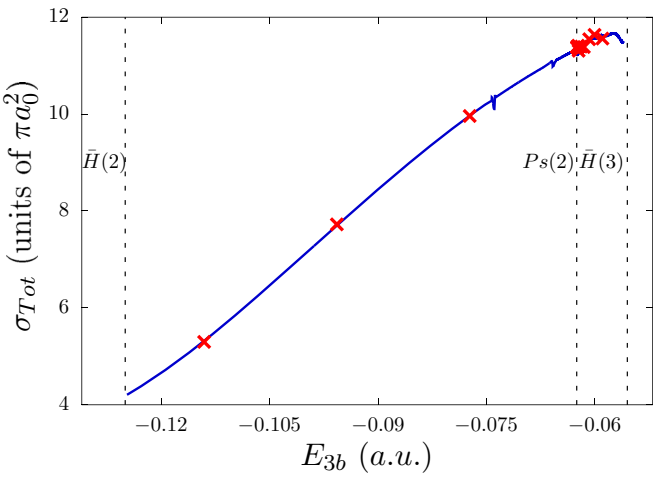

FIG. 11. Total cross section of the reaction $\bar{p} + \mathrm{Ps}(n = 1) \rightarrow e^- + \bar{\mathrm{H}}(n = 1,2)$. Crosses represent results from Ref. [16].

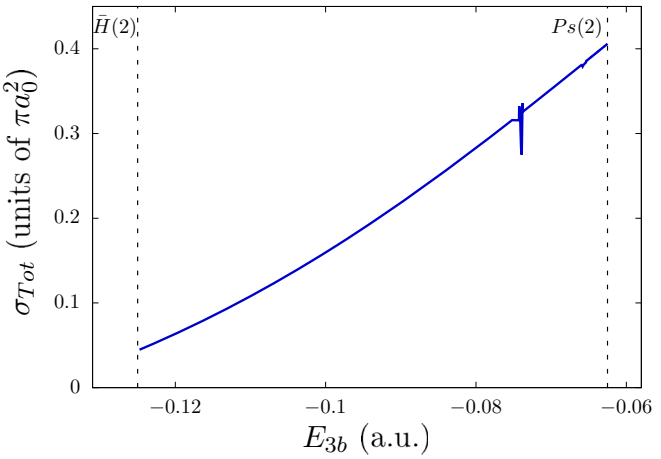

FIG. 12. Total cross section of the reaction $e^- + \bar{\mathrm{H}}(n = 1) \rightarrow e^- + \bar{\mathrm{H}}(n = 2)$.

below $10^{-2}\pi a_0$, which represents the accuracy of our calculation. Even though the contribution of Feshbach resonances seems to be very moderate in antihydrogen production, they demonstrate much more pronounced effects in other reactions, as is the case for the antihydrogen excitation cross section.

2. *Results between the* Ps($n = 2$) *and the* $\bar{\mathrm{H}}(n = 3)$ *thresholds*

Figure 13 presents the total cross section of antihydrogen production $\bar{\mathrm{H}}(1s,2s,2p)$ in $\bar{p} + \mathrm{Ps}(2s,2p)$ collisions. The higher contributions to the total cross section come from the D, F, and H partial waves. The Gailitis-Damburg oscillation coming from the S partial wave is drowned out by the importance of higher partial-wave cross sections. Nevertheless, the oscillating structures coming from the D partial wave remain noticeable. Their contribution is masked by the presence of other important partial waves, mostly H and F partial waves. Crosses represent the results obtained by Kadyrov *et al.* with the two-center convergent close-coupling method [16]. Triangles represent the results obtained by Hu *et al.* solving the

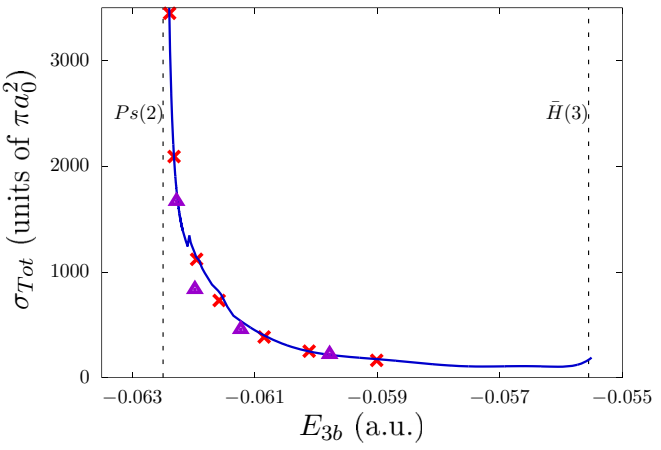

FIG. 13. Total antihydrogen production cross section from the $\bar{p} + \mathrm{Ps}(n = 2) \rightarrow e^- + \bar{\mathrm{H}}(n \leqslant 2)$ reaction. The blue line summarizes our calculations. Crosses and triangles represent results from Refs. [16] and [15], respectively.

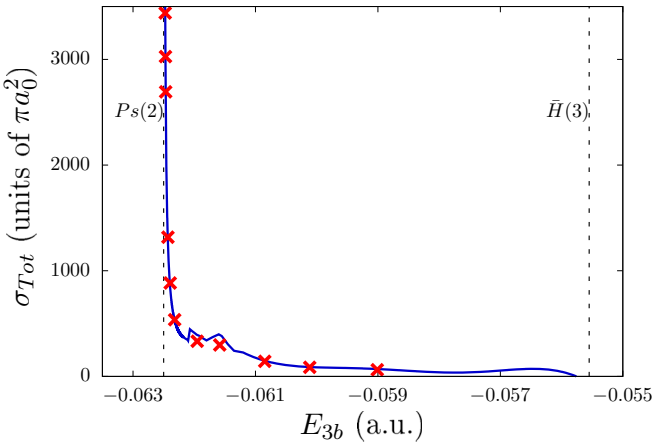

FIG. 14. Total cross section of the reaction $\bar{p} + \mathrm{Ps}(2p) \rightarrow e^- + \bar{\mathrm{H}}(n \leqslant 2)$. The blue line represents the results in this work; crosses, results from Ref. [16].

Faddeev-Merkuriev equations [15]. Our results are in excellent agreement with those of Kadyrov *et al.*

On the contrary, a discrepancy from Ref. [15] is observed in the D-wave oscillation area, between $E_{3b} = -0.062$ a.u. and $E_{3b} = -0.061$ a.u. Comparison of the cross sections by partial wave with those published in Table 1 of Ref. [15] points to the discrepancy in the D wave within the oscillation area and some disagreement in the H-wave cross section. Apart from these two differences, there is a very good agreement with the other partial cross sections calculated by Hu *et al.*

As GBAR considers the antihydrogen production from antiproton collisions with the positronium in the $2p$ state. The cross section of antihydrogen is given for this particular reaction in Fig. 14. The presence of both Gailitis-Damburg oscillations seems to enhance antihydrogen production. Our results are in good agreement with those in Ref. [16] with the exception of the two Gailitis-Damburg oscillations.

The total cross section of positronium production $\mathrm{Ps}(1s,2s,2p)$ in $e^- + \bar{\mathrm{H}}(2s,2p)$ collisions is presented in Fig. 15. The strongest contributions come from D, F, and H waves. Nevertheless the Gailitis oscillations from the S wave

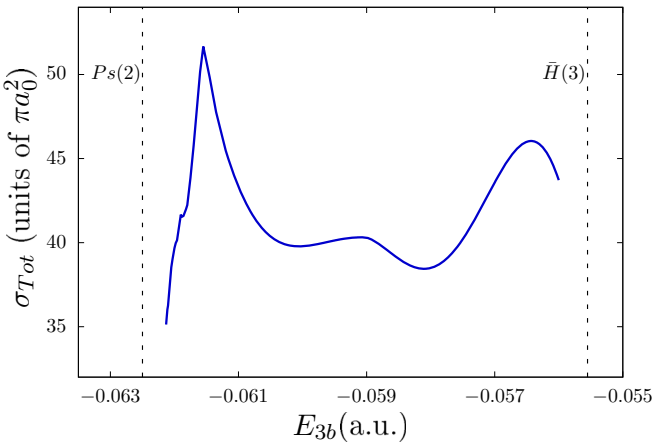

FIG. 15. Total cross section of the reaction $e^- + \bar{\mathrm{H}}(n = 2) \rightarrow \bar{p} + \mathrm{Ps}(n \leqslant 2)$.

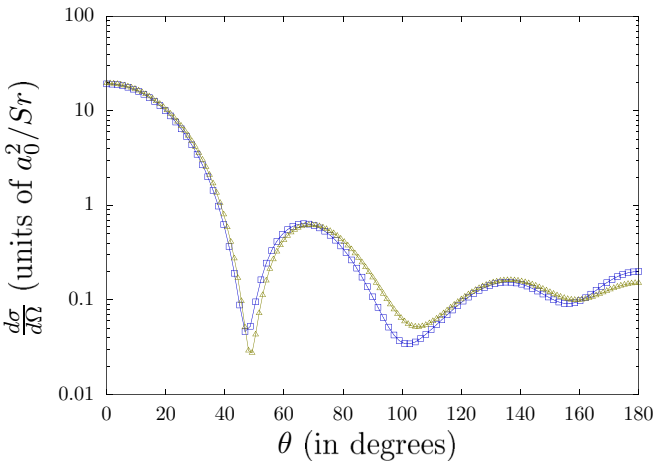

FIG. 16. Differential cross sections of the reaction $\bar{p} + \mathrm{Ps}(n = 1) \rightarrow e^- + \bar{\mathrm{H}}(n = 1)$ at $E_{3b} = -0.08$ a.u. (squares) and $E_{3b} = -0.115$ a.u. (triangles).

remain invisible, while the second oscillation coming from the D partial wave makes an important contribution.

C. Differential cross sections

Let us turn our attention to differential cross sections [Eq. (35)]. In Fig. 16 the differential cross sections for antihydrogen production $\bar{\mathrm{H}}(1s)$ in $\bar{p} + \mathrm{Ps}(1s)$ collisions are presented for two different energies, $E_{3b} = -0.08$ a.u. and $E_{3b} = -0.115$ a.u. The difference between both cross sections is rather mild. These results are in very good agreement with the results of Hu *et al.* presented in Fig. 2 of Ref. [24]. Let us remark that there is a very small difference, 2.7×10^{-4} a.u., between the energies presented in this paper and the energies chosen by Hu *et al.* To make a fair comparison the results in Fig. 16 were obtained by summing the partial waves for a total orbital momentum $0 \leqslant L \leqslant 4$.

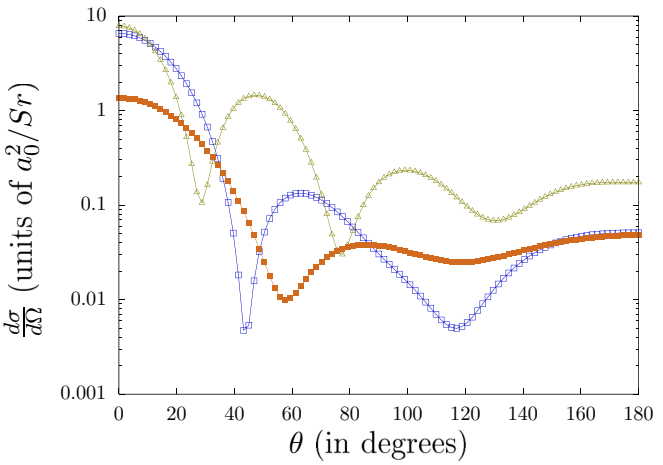

FIG. 17. Differential cross sections of the reaction $\bar{p} + \mathrm{Ps}(n = 1) \rightarrow e^- + \bar{\mathrm{H}}(n = 2)$ at $E_{3b} = -0.10$ a.u., $e^-(\ell_{y_1} = L) + \bar{\mathrm{H}}(2s)$ (open squares), $e^-(\ell_{y_1} = L - 1) + \bar{\mathrm{H}}(2p)$ (triangles), and $e^-(\ell_{y_1} = L + 1) + \bar{\mathrm{H}}(2p)$ (filled squares).

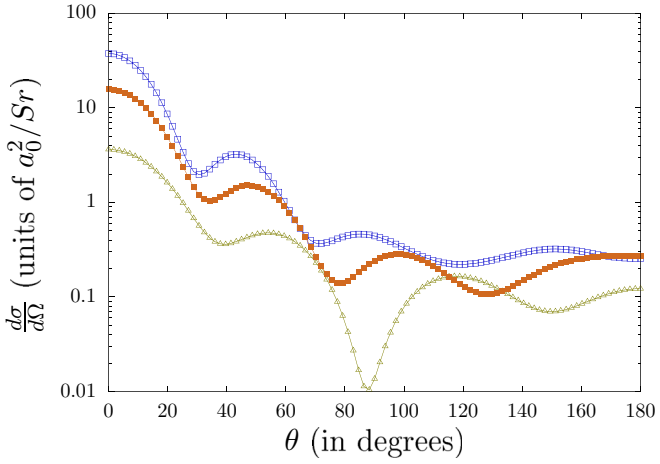

FIG. 18. Differential cross sections of the reaction $\bar{p} + \mathrm{Ps}(n = 1) \rightarrow e^- + \bar{\mathrm{H}}(n = 2)$ at $E_{3b} = -0.08$ a.u. (open squares), $E_{3b} = -0.10$ a.u. (filled squares), and $E_{3b} = -0.115$ a.u. (triangles).

In Fig. 17 the differential cross section for the different antihydrogen degenerated-state formations is plotted for energy $E_{3b} = -0.10$ a.u. by splitting it into three classes of partial waves, according to the relative angular momentum of the produced electron-antihydrogen pair. In this case we consider again contributions of all the partial waves up to a maximum total orbital momentum $L_{\max} = 7$. The curves in this figure can be compared to those obtained by Hu *et al.* [13] and presented in their Fig. 2. There is in general a good agreement between the two works. The positions of the minima coincide but there is a significant difference between their values, in particular, for the minimum in the $e^-(\ell_{y_1} = L + 1) + \bar{\mathrm{H}}$ formation. The value obtained by Hu *et al.* is close to 10^{-4}, whereas ours is close to 10^{-2}. In the $e^-(\ell_{y_1} = L) + \bar{\mathrm{H}}(2s)$ formation our minimum is weaker. In the case where $e^-(\ell_{y_1} = L - 1) + \bar{\mathrm{H}}$ the first and the last minima (30° and 130°) seem weaker than those obtained by Hu *et al.*, while the second minimum (80°) seems a bit stronger.

In Fig. 18 the antihydrogen $\bar{\mathrm{H}}(2s,2p)$ production in $\bar{p} + \mathrm{Ps}(1s)$ collisions is shown for three energies. As shown, in contrast to the $\bar{\mathrm{H}}(1s)$ production differential cross section (Fig. 16), the $\bar{\mathrm{H}}(2s,2p)$ production (Fig. 18) is much more sensitive to an energy variation. As there is a small difference between our energy ($E_{3b} = -0.10$ a.u.) and that in Ref. [13] ($E_{3b} = -0.099\,725$ a.u.), this sensitivity may explain the difference between the minima obtained in the two works. In addition, while the differential cross section increases with energy, its distribution at backward angles flattens.

V. CONCLUSION

In this paper a method for solving Faddeev-Merkuriev equations using the Lagrange-mesh method is presented and applied to describe collisions involving the $(\bar{p},e^+,e^-)$ three-body system. This system is studied in detail in the energy range between the $e^- + \bar{\mathrm{H}}(n = 2)$ and the $e^- + \bar{\mathrm{H}}(n = 3)$ thresholds, aiming to provide antihydrogen production cross sections for future experiments (GBAR, AEGIS, etc.) on antimatter. Special emphasis is placed on the role played by Feshbach resonances and Gailitis-Damburg oscillations. We have examined two Feshbach resonances, the first in the S partial wave and the second in the P partial wave. In $\bar{p} + \mathrm{Ps}(n = 2) \rightarrow e^- + \bar{\mathrm{H}}(n = 2)$ scattering cross sections we have been able to highlight four Gailitis-Damburg oscillations, two in the S partial wave and, for the first time, two in the D partial wave. We have also found, for the first time, a Gailitis-Damburg oscillation in the P-wave partial cross section of antihydrogen excitation $e^- + \bar{\mathrm{H}}(n = 1) \rightarrow e^- + \bar{\mathrm{H}}(n = 2)$. The Gailitis-Damburg oscillations found in the D partial wave can also be observed in the partial cross section of the reaction $e^- + \bar{\mathrm{H}}(n = 2) \rightarrow \bar{p} + \mathrm{Ps}(n = 2)$, where the contribution of one of the oscillations seems to be of greater importance. In addition to the new oscillations observed, our results are in very good agreement with the previous works while giving more detailed cross sections. Nevertheless, the observed resonances or oscillations may only play a minor role in enhancing antihydrogen production in the GBAR experiment. Feshbach resonances are too narrow, whereas Gailitis-Daburg oscillations are exhibited at an energy too low to be considered during this project.

ACKNOWLEDGMENTS

We thank P. Comini for useful discussions. This work was granted access to the HPC resources of TGCC/IDRIS under allocation 2016-x2016056006 made by Grand Equipement National de Calcul Intensif (GENSI). Some of the calculations were also realized at High-Performance-Computing Center of the University of Strasbourg.

[1] T. A. Wagner, S. Schlamminger, J. Gundlach, and E. Adelberger, Class. Quantum Grav. **29**, 184002 (2012).
[2] J. D. Tasson, Int. J. Mod. Phys. **30**, 1460273 (2014).
[3] P. Debu, J. Phys. Conf. Ser. **460**, 012008 (2013).
[4] E. Gibney, Nature **548**, 20 (2017).
[5] J. Walz and T. Hänsch, Gen. Relat. Gravit. **36**, 561 (2004).
[6] C. H. Storry, A. Speck, D. L. Sage, N. Guise, G. Gabrielse, D. Grzonka, W. Oelert, G. Schepers, T. Sefzick, H. Pittner *et al.* (ATRAP Collaboration), Phys. Rev. Lett. **93**, 263401 (2004).
[7] M. Gailitis, J. Phys. B **15**, 3423 (1982).
[8] R. Lazauskas, P.-A. Hervieux, M. Dufour, and M. Valdes, J. Phys. B **49**, 094002 (2016).
[9] C.-Y. Hu, D. Caballero, and Z. Papp, Phys. Rev. Lett. **88**, 063401 (2002).
[10] M. Gailitis and Damburg, R. Sov. Phys. JETP **17**, 1107 (1963).
[11] N. Levinson, Kgl. Danske Videnskab. Selskab, Math-fys. Medd. **25**, No. 9 (1949).
[12] P. Comini and P.-A. Hervieux, New J. Phys. **15**, 095022 (2013).
[13] C.-Y. Hu, D. Caballero, and Z. Hlousek, J. Phys. B **34**, 331 (2000).
[14] C.-Y. Hu, D. Caballero, and Z. Hlousek, J. Mod. Phys. **4**, 622 (2013).
[15] C.-Y. Hu and D. Caballero, J. Phys. B **35**, 3879 (2002).

[16] A. S. Kadyrov, C. M. Rawlins, A. T. Stelbovics, I. Bray, and M. Charlton, Phys. Rev. Lett. **114**, 183201 (2015).
[17] C. M. Rawlins, A. S. Kadyrov, A. T. Stelbovics, I. Bray, and M. Charlton, Phys. Rev. A **93**, 012709 (2016).
[18] I. I. Fabrikant, A. W. Bray, A. S. Kadyrov, and I. Bray, Phys. Rev. A **94**, 012701 (2016).
[19] D. Baye, Phys. Status Solidi B **243**, 1095 (2006).
[20] D. Baye, Phys. Rep. **565**, 1 (2015).
[21] L. D. Faddeev, Sov. Phys. JETP **12**, 1014 (1961).
[22] S. Merkuriev, Acta Phys. Austriaca Suppl. **XXIII**, 65 (1981).
[23] L. Faddeev and S. Merkuriev, *Quantum Scattering Theory for Several Particle Systems* (Kluwer, Dordrecht, Netherlands, 1993), Chap. 7.
[24] C.-Y. Hu, J. Phys. B **32**, 3077 (1999).
[25] A. Kievsky, M. Viviani, P. Barletta, C. Romero-Redondo, and E. Garrido, Phys. Rev. C **81**, 034002 (2010).
[26] J. Friar and G. Payne, Few-Body Syst. **33**, 233 (2003).
[27] R. Lazauskas, Ph.D. thesis, Université Joseph Fourier, Grenoble (2003), https://hal.archives-ouvertes.fr/tel-00004178.
[28] The positions of these resonances could not be calculated independently in this work; one is obliged to scan the entire region by scattering calculations and check for rapid variation in the cross section.
[29] M. Umair and S. Jonsell, J. Phys. B **47**, 225001 (2014).
[30] A. I. Baz, Ya. B. Zel' dovich, and A. M. Perelomov, *Scattering, Reaction in Non-Relativistic Quantum Mechanics* (Jerusalem, 1969).
[31] Z. Papp, C.-Y. Hu, Z. T. Hlousek, B. Kónya, and S. L. Yakovlev, Phys. Rev. A **63**, 062721 (2001).
[32] C.-Y. Hu, Phys. Rev. A **59**, 4813 (1999).